

Multihadron-event properties in e^+e^- annihilation at $\sqrt{s} = 52-57$ GeV

Y. K. Li,^{a,d} J. Li,^a C. P. Cheng,^a P. Gu,^a M. H. Ye,^a Y. C. Zhu,^a
 R. Imlay,^b P. Kirk,^b J. Lim,^b R. R. McNeil,^b W. Metcalf,^b S. S. Myung,^b A. Abashian,^c
 K. Gotow,^c K. P. Hu,^c E. H. Low,^c M. E. Mattson,^c L. Piilonen,^c K. L. Sterner,^c
 S. Lusin,^d C. Rosenfeld,^d A. T. M. Wang,^d S. Wilson,^d M. Frautschi,^e H. Kagan,^e
 R. Kass,^e C. G. Trahern,^e R. E. Breedon,^{f,g} G. N. Kim,^{f,g} Winston Ko,^f R. L. Lander,^f
 K. Maeshima,^f R. L. Malchow,^f J. R. Smith,^f D. Stuart,^f K. Abe,^g Y. Fujii,^g
 Y. Higashi,^g S. K. Kim,^g Y. Kurihara,^g A. Maki,^g T. Nozaki,^g T. Omori,^g H. Sagawa,^g
 Y. Sakai,^g Y. Sugimoto,^g Y. Takaiwa,^g S. Terada,^g R. C. Walker,^{g,o} F. Kajino,ⁱ
 D. Perticone,^j R. Poling,^j T. Thomas,^j Y. Ishi,^k K. Miyano,^k H. Miyata,^k T. Sasaki,^k
 Y. Yamashita,^l A. Bacala,^{m,n} J. Liu,^m I. H. Park,^m F. Sannes,^m S. Schnetzer,^m R. Stone,^m
 J. Vinson,^m P. Auchincloss,^o D. Blanis,^o A. Bodek,^o H. Budd,^o S. Eno,^o C. A. Fry,^{o,g}
 H. Harada,^o Y. H. Ho,^o Y. K. Kim,^o T. Kumita,^o T. Mori,^o S. L. Olsen,^{o,h} N. M. Shaw,^o
 A. Sill,^o E. H. Thorndike,^o K. Ueno,^o H. W. Zheng,^o S. Kobayashi,^p A. Murakami,^p
 J. S. Kang,^q H. J. Kim,^q M. H. Lee,^q D. H. Han,^r E. J. Kim,^r D. Son,^r T. Kojima,^s
 S. Matsumoto,^s R. Tanaka,^s Y. Yamagishi,^s T. Yasuda,^s T. Ishizuka,^t and K. Ohta^t

(The AMY Collaboration)

^a*Institute of High Energy Physics, Beijing, 100039*

^b*Louisiana State University, Baton Rouge, Louisiana 70803*

^c*Virginia Polytechnic Institute and State University, Blacksburg, Virginia 24061*

^d*University of South Carolina, Columbia, South Carolina 29208*

^e*Ohio State University, Columbus, Ohio 43210*

^f*University of California, Davis, California 95616*

^g*KEK, National Laboratory for High Energy Physics, Ibaraki 305,*

^h*Tsukuba University, Ibaraki 305,*

ⁱ*Konan University, Kobe 658,*

^j*University of Minnesota, Minneapolis, Minnesota 55455*

^k*Niigata University, Niigata 950-21,*

^l*Nihon Dental College, Niigata 951,*

^m*Rutgers University, Piscataway, New Jersey 08854*

ⁿ*University of the Philippines, Quezon City, 3004*

^o*University of Rochester, Rochester, New York 14627*

^p*Saga University, Saga 840,*

^q*Korea University, Seoul 136-701,*

^r*Kyungpook National University, Taegu 702-701,*

^s*Chuo University, Tokyo 112,*

^t*Saitama University, Urawa 338,*

(Received 20 November 1989)

We present the general properties of multihadron final states produced by e^+e^- annihilation at center-of-mass energies from 52 to 57 GeV in the AMY detector at the KEK collider TRISTAN. Global shape, inclusive charged-particle, and particle-flow distributions are presented. Our measurements are compared with QCD+fragmentation models that use either leading-logarithmic parton-shower evolution or QCD matrix elements at the parton level, and either string or cluster fragmentation for hadronization.

I. INTRODUCTION

Quantum chromodynamics (QCD), the gauge theory of colored quarks and gluons, was introduced to explain the properties of hadrons. QCD has subsequently become the accepted theory of the strong interaction. However, it remains the least quantitatively tested part of the so-called standard model of elementary-particle physics, i.e.,

the standard (Glashow-Salam-Weinberg) electroweak model¹ and QCD (Ref. 2). In particular, the transition from partons to the observable hadrons is, as yet, not well understood. There has been progress in recent years in the development of models of the process $e^+e^- \rightarrow \gamma^*/Z^* \rightarrow$ hadrons that generate partons according to perturbative QCD and which then follow a phenomenological hadronization scheme for the metamorphosis of

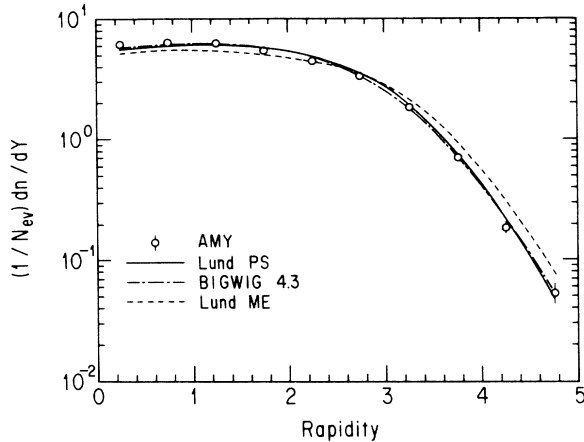


FIG. 1. The rapidity distribution of charged particles with respect to the thrust axis and predictions of the models.

the partons into hadrons. These QCD+fragmentation models have helped experimenters correct their data and plumb the underlying parton structure and have helped provide a framework to understand better the long-range behavior of the strong interaction.

In the previous ten years, many studies of hadron production in e^+e^- annihilation have been performed. These comparisons of data from the SLAC and DESY storage rings PEP and PETRA with QCD+fragmentation models have been made in the energy region $12.0 < \sqrt{s} < 43$ GeV (Refs. 3–6). Over time, the models have been updated and refined with the intention of obtaining better agreement with experimental results. The arbitrary parameters of the models have recently been tuned to obtain the best description of Mark II data⁵ at 29 GeV and of TASSO data⁶ at 35 GeV. Generally, the strongest candidate models have been successful in reproducing most features of these data, but a more rigorous

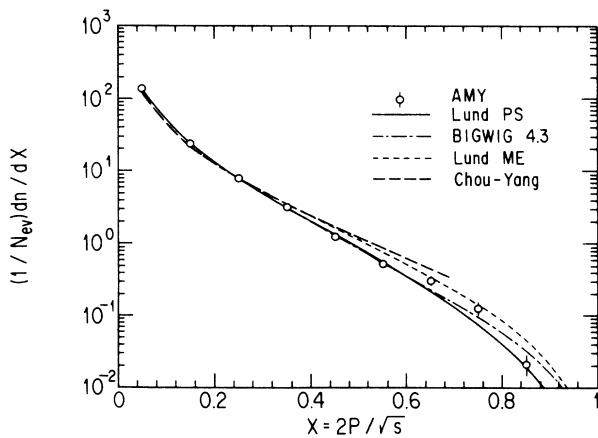


FIG. 2. The charged-particle X distribution and predictions of the models.

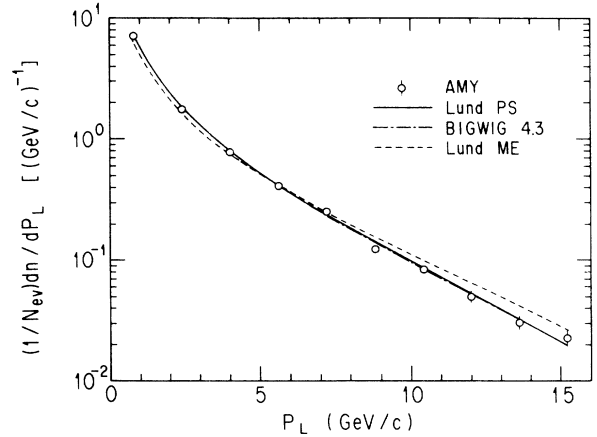


FIG. 3. The P_L distribution of charged particles with respect to the sphericity axis and predictions of the models.

test is to check the accuracy of a model's description of data at energies other than that for which the parameters were tuned.

The AMY detector⁷ at the KEK storage ring TRISTAN has accumulated more than 2000 events with multihadron final states produced by e^+e^- annihilation at center-of-mass energies between 52 and 57 GeV. In this paper we present the general properties of these events, and compare the corrected data to different QCD+fragmentation models using values of the parameters tuned with data from the lower-energy experiments. The charged-particle multiplicities are described in a separate report.⁸ In Sec. II we briefly describe the QCD+fragmentation models that we used to compare with our data. The definitions for global event-shape and inclusive particle properties form Sec. III. A description of the AMY detector and the particle and event-selection criteria are given in Secs. IV and V, respectively. In Sec.

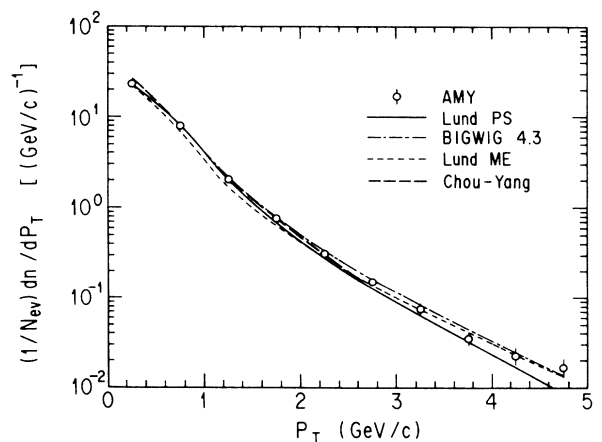


FIG. 4. The P_T distribution of charged particles with respect to the sphericity axis and predictions of the models.

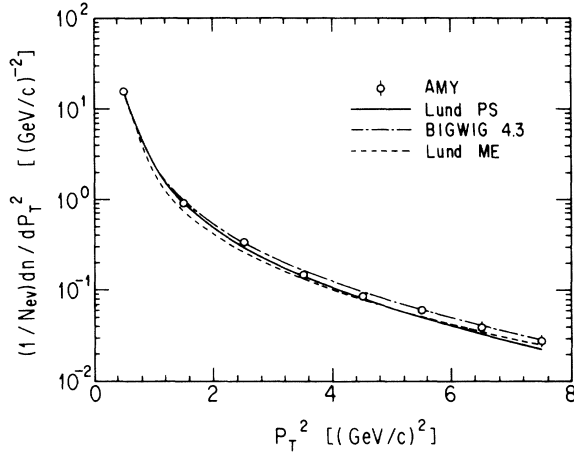


FIG. 5. The P_T^2 distribution of charged particles with respect to the sphericity axis and predictions of the models.

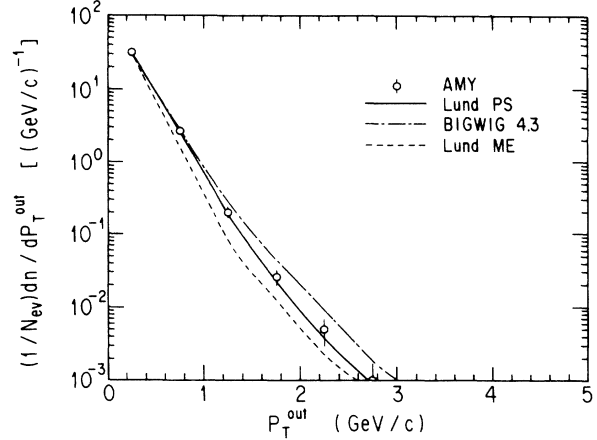


FIG. 7. The P_T^{out} distribution of charged particles with respect to the event plane and predictions of the models.

VI the data correction and error estimation are described. The results of the comparison between data and the models at the luminosity-weighted average center-of-mass energy of 55.2 GeV are given in Sec. VII. Section VIII contains the summary and conclusion.

II. QCD+FRAGMENTATION MODELS

Present QCD+fragmentation models can in general be divided with respect to their application of QCD calculations into two classes: those in which parton distributions are generated following leading-logarithm parton-shower evolution and those in which they are produced according to QCD matrix elements. Fragmentation of the partons into hadrons follows, usually employing one of three mechanisms: string, cluster, or independent

fragmentation, the last of which is disfavored by experiments at PETRA and PEP energies⁹ and will therefore not be considered further.

Because of their complexity, fragmentation models are now almost exclusively implemented via Monte Carlo techniques in computer programs. This also enables the experimenter to pass events generated by a particular model through a detector simulation allowing close comparison between models and data. In this paper, we compare AMY data to distributions generated by three of the most widely used QCD+fragmentation model programs: the Lund JETSET program version 6.2, incorporating matrix-element calculations¹⁰ and the Lund parton-shower model in version 6.3 (Ref. 11), both with string fragmentation,¹² and the Marchesini-Webber parton-shower and cluster-decay program BIGWIG 4.3. Important features of these models are briefly discussed below.¹³

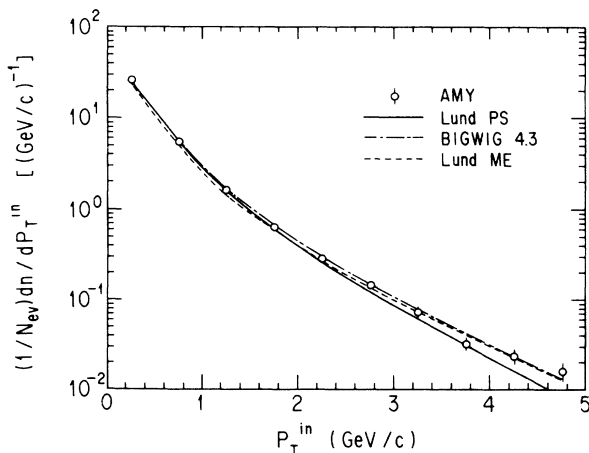


FIG. 6. The P_T^{in} distribution of charged particles with respect to the sphericity axis in the event plane and predictions of the models.

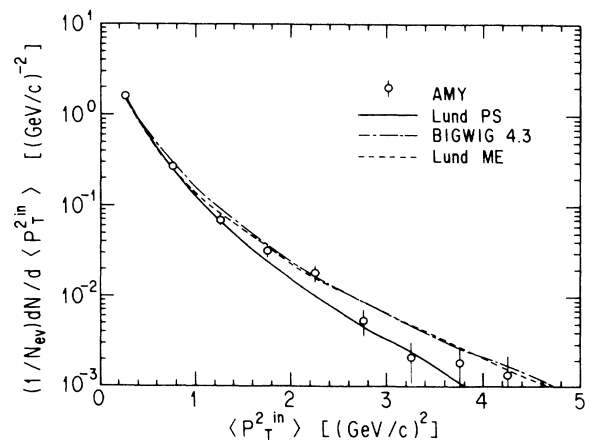


FIG. 8. The $\langle P_T^{in} \rangle$ distribution and predictions of the models.

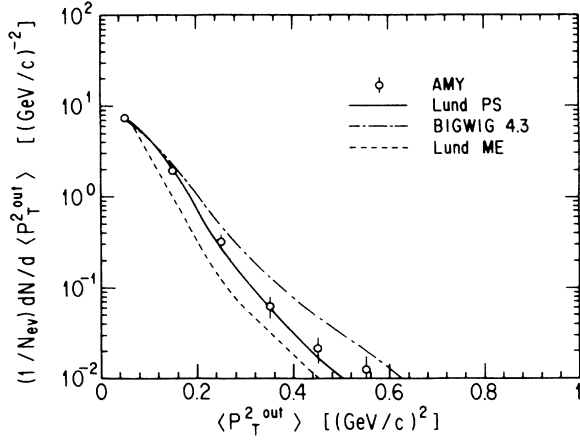


FIG. 9. The $\langle P_T^{2, \text{out}} \rangle$ distribution and predictions of the models.

A. The Lund matrix-element model (Ref. 14)

QCD matrix-element predictions for the production of two-, three-, and four-parton final states ($e^+e^- \rightarrow q\bar{q}, q\bar{q}g, q\bar{q}gg, q\bar{q}q\bar{q}$), calculated up to second order of α_s , are used by this model. To first order, the model uses

$$\alpha_s = \frac{12\pi}{(33 - 2n_f) \ln(Q^2/\Lambda_{\overline{\text{MS}}}^2)},$$

where n_f is the number of active flavors and $\Lambda_{\overline{\text{MS}}}$ is one of the parameters of the model ($\overline{\text{MS}}$ denotes the modified minimal-subtraction scheme). To avoid divergences in the Monte Carlo generation, three-parton events in which one parton is a collinear or soft gluon are merged with the two-parton events. This cutoff is given in terms of the parameter y_{min} , which specifies the minimum required invariant mass squared of any two partons i and j in an event as a fraction of s , the total center-of-mass en-

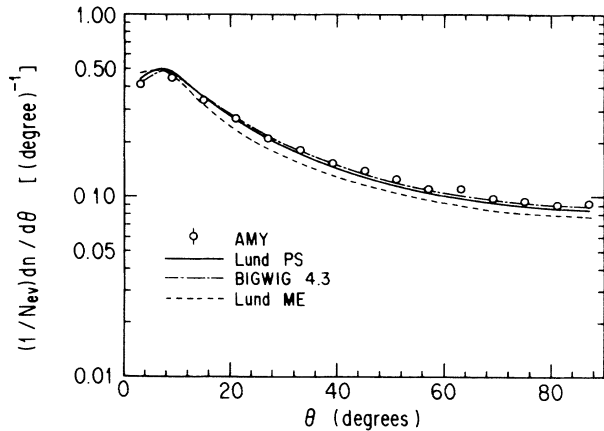


FIG. 10. The charged-particle flow with respect to the sphericity axis and predictions of the models.

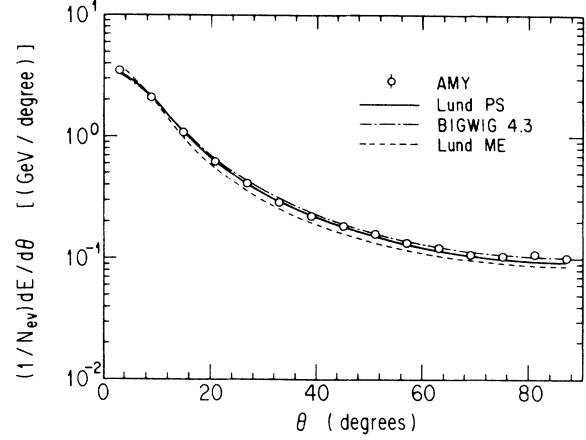


FIG. 11. The energy flow with respect to the sphericity axis and predictions of the models.

ergy squared ($M_{ij}^2 > y_{\text{min}}s$). As has been observed,^{15–17} the Lund matrix-element model, which allows states with at most four partons, fails to reproduce the rates for four- or five-jet-like events. At lower energies, second-order matrix elements appear to be sufficient, but this deficiency begins to become evident at PETRA and PEP energies. Because of the complexity of calculation to third order, simulation programs which include higher-order QCD contributions to jet cross sections are not available.

Following parton generation, hadrons are formed according to a string fragmentation scheme.¹² A string is stretched between the final quarks forming a color-singlet system and is allowed to break by forming additional color-singlet quark pairs. Gluons are treated as kinks on the string between the quark ends with associated energy and momentum, and are therefore attached to two strings corresponding to the gluon's double color charge. The

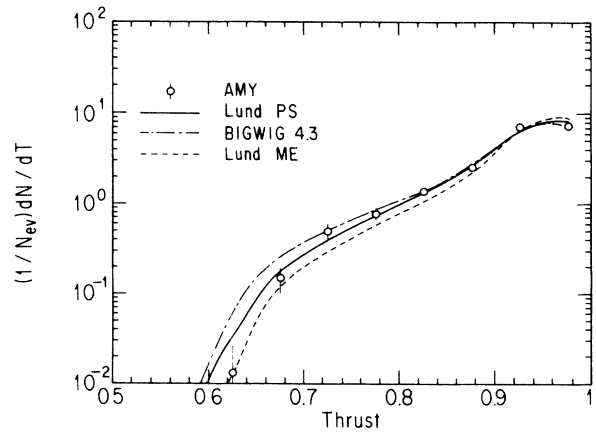


FIG. 12. The thrust distribution and predictions of the models.

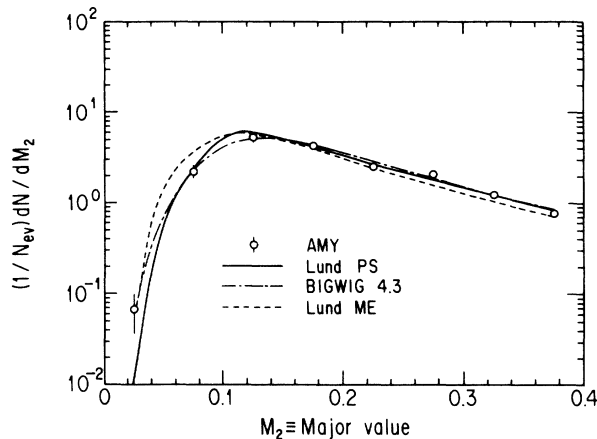


FIG. 13. The major-value distribution and predictions of the models.

longitudinal component of the momenta of the final-state hadrons formed in the fragmentation process is distributed according to the symmetric fragmentation function

$$f(z) = \frac{(1-z)^a}{z} e^{-bm_T^2/z},$$

where m_T is the transverse mass of the hadron ($m_T^2 = m^2 + P_T^2$) and z is the fraction of the primordial parton energy it carries. Each primary quark is assigned a transverse momentum following a Gaussian spectrum $\sim \exp(-P_T^2/2\sigma_q^2)$. The fragmentation parameters a , b , and σ_q are relevant to such inclusive global properties as multiplicities and rapidity distributions. These parameters are in addition to the basic model parameters $\Lambda_{\overline{\text{MS}}}$ and y_{min} .

B. The Lund parton-shower model (Refs. 11 and 18)

To compensate for insufficient knowledge of the higher-order contributions to multijet cross sections, a

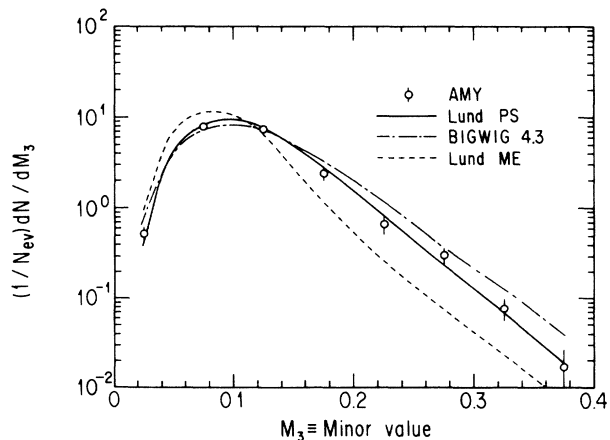


FIG. 14. The minor-value distribution and predictions of the models.

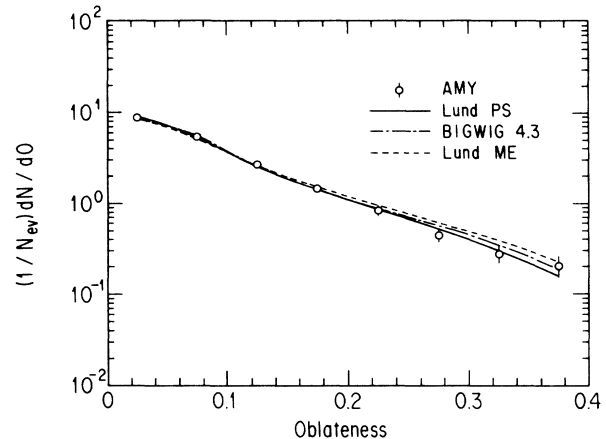


FIG. 15. The oblateness distribution and predictions of the models.

“shower” process¹⁹ was conceived in order to calculate parton distributions during jet development to approximately full order. This treatment of multijet configurations is based on the QCD leading-logarithm approximation (LLA) and, as incorporated into JETSET 6.3, it is known as the Lund parton-shower (PS) model. The Lund PS is one of the more popularly used shower models, and it contains an option for including soft-gluon interference effects.

In the PS scheme, a cascade evolves according to the Altarelli-Parisi equations²⁰ based on LLA calculations. The interference effects are realized by angular ordering, which is imposed by a rejection technique.¹⁸ For the initial branching, the partons are distributed following first-order matrix elements and no angular ordering is applied. A branching is halted when its virtuality reaches some minimum value Q_0 the shower virtuality cutoff, which is one of the important parameters of the model. Another relevant parameter is the QCD LLA scale value Λ_{LLA} and the default Q^2 scale for α_s is retained ($Q^2 \simeq P_T^2$). At

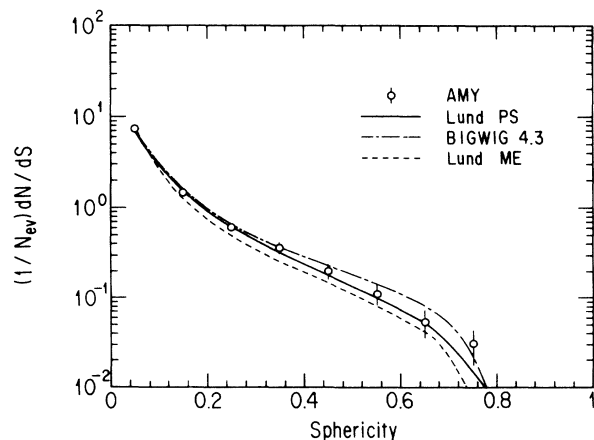


FIG. 16. The sphericity distribution and predictions of the models.

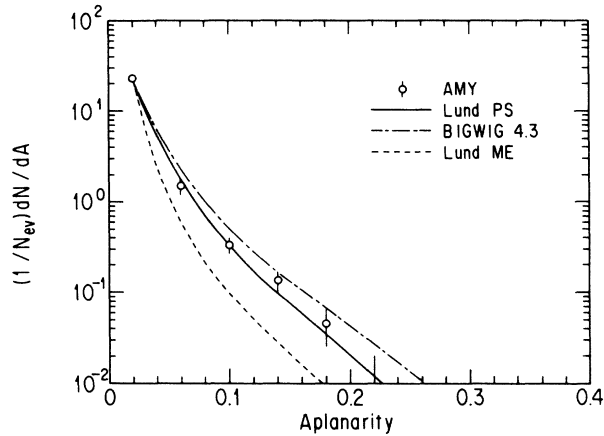


FIG. 17. The aplanarity distribution and predictions of the models.

the end of parton production, fragmentation proceeds as described in the previous section, and so the model also uses the above-mentioned string fragmentation parameters.

C. The Webber model (Refs. 21 and 22)

The Webber model employs leading-logarithmic parton-shower evolution and includes soft-gluon interference effects by angular ordering of successive gluon branchings. A highly virtual $q\bar{q}$ pair is generated and allowed to radiate gluons, which subsequently branch into more gluons or $q\bar{q}$ pairs according to the leading-logarithmic QCD probabilities. The branching stops when the parton virtuality becomes less than the cutoff parameter Q_0 . The initial $q\bar{q}$ pair is boosted to a frame in which the initial opening angle is 90° . As a consequence, unlike the Lund parton-shower approach, the Webber

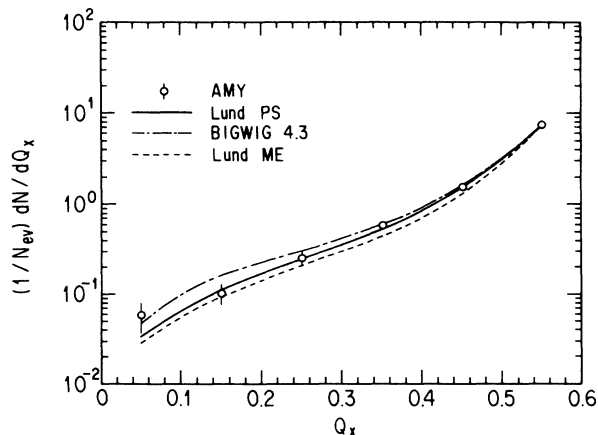


FIG. 18. The Q_x distribution and predictions of the models.

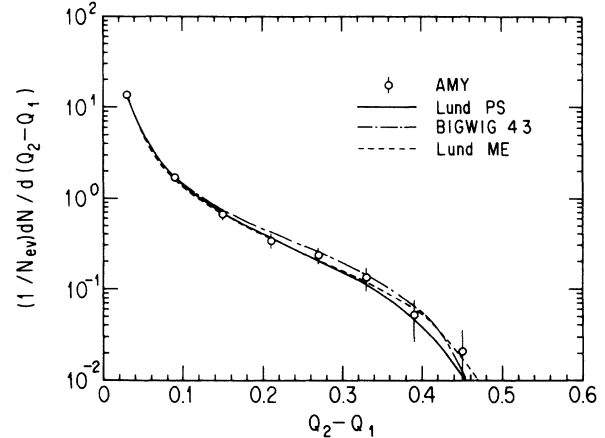


FIG. 19. The $Q_2 - Q_1$ distribution and predictions of the models.

model is not manifestly covariant. In addition, the mass of the initial parton cannot be given in advance, but must be reconstructed following the termination of the cascade evolution. In this model, also, the Q^2 scale is chosen to be $Q^2 \simeq P_T^2$.

At the end of the cascade, when all partons have been put on the mass shell, the gluons are split into $q\bar{q}$ pairs, and each parton then joins with a neighbor of the correct color index to form a color-singlet cluster. The clusters for which the mass exceeds a certain value, m_c , are split into two, and all clusters are allowed to decay via a phase-space model into resonances or stable particles.

The Webber fragmentation scheme is incorporated into the programs BIGWIG and HERWIG, the latter intended to be a general-purpose event generator able to simulate lepton-hadron and hadron-hadron scattering as well as e^+e^- collisions. There are some differences in such details as cluster decay between the two programs.²² There are three important arbitrary parameters in the Webber model: the cascade virtuality cutoff Q_0 , the LLA QCD

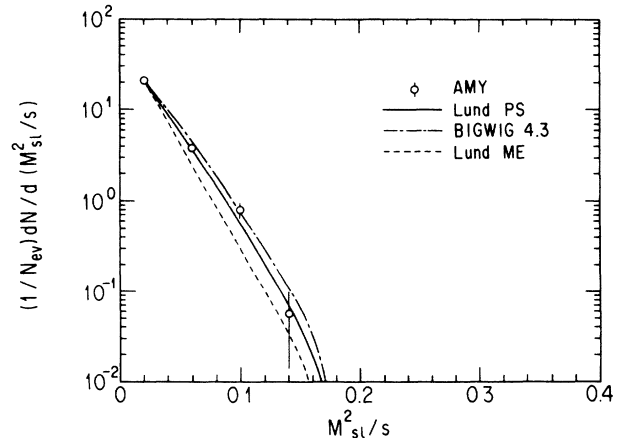


FIG. 20. The M_{sl}^2/s distribution and predictions of the models.

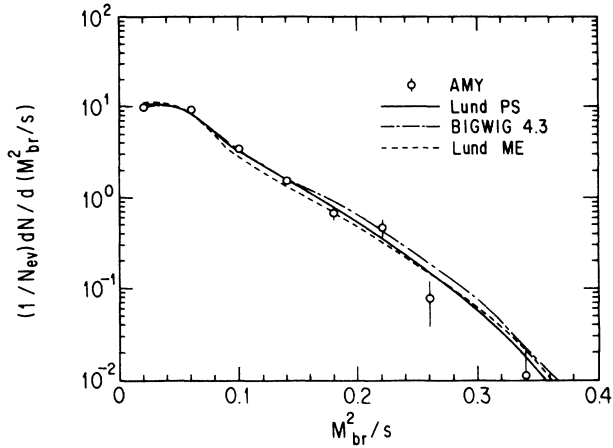


FIG. 21. The M_{br}^2/s distribution and predictions of the models.

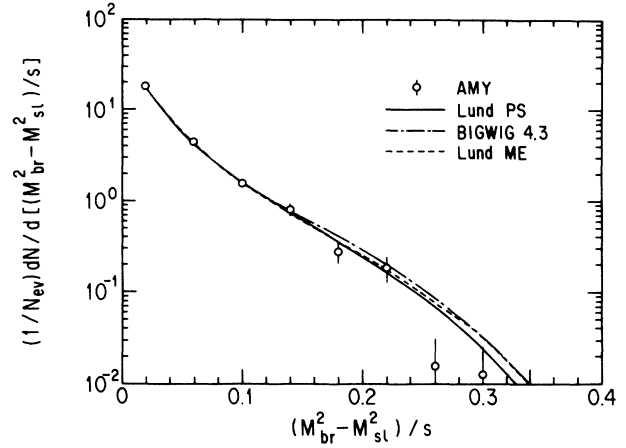


FIG. 22. The $(M_{br}^2 - M_{si}^2)/s$ distribution and predictions of the models.

scale parameter Λ_{LLA} , and the cluster mass parameter m_c .

III. OBSERVABLES IN ANALYSIS OF MULTIHADRON-EVENT PROPERTIES

Events are characterized according to their shape in momentum space by the eigenvalues of the sphericity tensor,

$$S_{\alpha\beta} = \frac{\sum P_{i\alpha} P_{i\beta}}{\sum |\mathbf{P}_i|^2},$$

in which $\alpha, \beta = 1, 2, 3$ and the sums are over all particles i in an event. The eigenvalues Q_1, Q_2, Q_3 (ordered such that $Q_1 < Q_2 < Q_3$ and normalized so that $Q_1 + Q_2 + Q_3 = 1$) and the corresponding principal axes $\mathbf{n}_1, \mathbf{n}_2, \mathbf{n}_3$ of the momentum ellipsoid are determined for each event. The sphericity axis \mathbf{n}_3 defines the event axis and the event plane is given by $(\mathbf{n}_2, \mathbf{n}_3)$. Because the sphericity tensor uses the momenta of the particles quadratically, the high-momentum particles in an event will contribute more strongly to observables derived from this tensor than to those which use the momenta linearly.

A measure of event structure that uses the linear momenta is the thrust

$$T = \max \frac{\sum |\mathbf{P}_{iL}|}{\sum |\mathbf{P}_i|},$$

the thrust axis being chosen to maximize $\sum |\mathbf{P}_{iL}|$, the sum of the components of the momenta parallel to the thrust axis of all particles in an event. Extreme two-jet events with completely collinear final-state particles would have $T = 1$, and those completely isotropic would have $T = \frac{1}{2}$.

All observed charged and neutral particles, which were selected as described in Sec. V, are included in the determination of event shapes, axes, and jet masses. The observables used in our measurement are defined as follows.

(a) The charged-particle rapidity with respect to the thrust axis is defined as $Y = \frac{1}{2} \ln[(E + P_L)/(E - P_L)]$, where E is the particle energy and P_L is the component of the momentum parallel to the thrust axis.

(b) The scaled track momentum $X = 2P/\sqrt{s}$ is one common fragmentation variable for charged particles that is used in this analysis.²³

(c) There are several charged-particle transverse momentum variables derived from the sphericity tensor. P_T is the charged-particle momentum transverse to the sphericity axis and P_T^2 is its square. P_T^{in} and P_T^{out} are, respectively, the charged-particle transverse momenta in and out of the event plane, while $\langle P_T^{\text{in}2} \rangle = \langle P^2 \rangle Q_2$ and $\langle P_T^{\text{out}2} \rangle = \langle P^2 \rangle Q_1$.

(d) The charged-particle flow is defined as $dn/d\theta$, where θ is the angle between the particle and the sphericity axis. The energy flow $dE/d\theta$ is also used, defined by weighting $dn/d\theta$ by the energies of the charged and neutral particles.

TABLE I. Parameters for the Lund matrix-element model

	Default	Mark II	AMY tuned ^a
$\Lambda_{\overline{MS}}$ (GeV)	0.50	0.50	0.82
y_{\min}	0.02	0.015	0.02
Fragmentation parameter a	1.0	0.9	0.9
Fragmentation parameter b (GeV ⁻²)	0.7	0.7	0.45
Gaussian P_T parameter $\sqrt{2}\sigma_q$ (GeV/c)	0.40	0.33	0.41

^aY. K. Li *et al.*, AMY Internal Report No. 480, 1989 (unpublished).

TABLE II. Parameters for the Lund parton-shower model.

	Default	Mark II
Λ_{LLA} (GeV)	0.40	0.40
Cascade virtuality cutoff Q_0 (GeV)	1.0	1.0
Fragmentation parameter a	0.50	0.45
Fragmentation parameter b (GeV ⁻²)	0.9	0.9
Gaussian P_T parameter $\sqrt{2}\sigma_q$ (GeV/c)	0.35	0.33

(e) Thrust distributions are also used. The axis perpendicular to the thrust axis with the greatest thrust value is defined to be the major axis, and the sum of longitudinal momenta with respect to this axis over the sum of momenta is the major value. The minor axis is assigned so as to form an orthonormal system, and the minor value is the thrust value along this axis. The difference between the major and minor values is the oblateness. These observables use momenta linearly, and are therefore more sensitive to soft particle production than those derived from sphericity analysis.

(f) The sphericity is defined as $S = \frac{3}{2}(Q_1 + Q_2)$. Ideal two-jet events would have $S = 0$, while S would equal unity for completely isotropic events. Aplanarity, $A = \frac{3}{2}Q_1$, and the variables $Q_x = (1/\sqrt{3})(Q_3 - Q_2)$ and $Q_2 - Q_1$ are also used.

(g) The event may be divided into hemispheres by the plane perpendicular to the sphericity axis, and the total invariant mass of all particles in each hemisphere calculated. The scaled jet invariant mass squared of each of the hemispheres of an event is a well-behaved quantity in perturbation calculations. The smaller of the two values defines M_{sl} , the mass of the slim jet, and the other defines M_{br} , the mass of the broad jet. The scaled quantities of interest are M_{sl}^2/s , M_{br}^2/s , and $(M_{sl}^2 - M_{br}^2)/s$ (Ref. 23).

IV. DETECTOR DESCRIPTION

The complete AMY detector, trigger, and luminosity measurements are described elsewhere.⁷ Here we mention only those features which are essential for multihadron-event analysis. The AMY detector consists of a tracking detector and shower counter inside a 3-T solenoid magnetic coil which is surrounded by a steel flux return yoke followed by a muon detection system. The charged-particle tracking detector consists of a 4-layer cylindrical array of drift tubes (inner tracking chamber, or ITC) and a 40-layer cylindrical drift chamber (central drift chamber, or CDC) with 25 axial layers of wires and 15 stereo layers. Charged particles are detected efficiently over the polar angle region $|\cos\theta| < 0.87$ with a momentum resolution $\Delta P_t/P_t = 0.7\% \times [P_t \text{ (GeV/c)}]$.

Radially outside of the CDC is a 15-radiation-length cylindrical electromagnetic calorimeter (barrel shower counter, or SHC) which serves as a photon detector. The detector fully covers the angular region $|\cos\theta| < 0.73$. The energy resolution is $\sigma_E/E \approx 23\%/\sqrt{E \text{ (GeV)}} + 6\%$ and its angular resolution is $\sigma_\phi \approx 0.23^\circ$ and $\sigma_\theta \approx 0.3^\circ$. In the end-cap region, there is an electromagnetic calorimeter specialized for measuring Bhabha scattering.

V. EVENT SELECTION AND BACKGROUND

Charged tracks were required to have at least eight axial and five stereo hits in the CDC that fit to a helix. Showers were associated with each energy cluster in the SHC having more than 0.2 GeV. Any shower with energy less than 1 GeV and within 2° of the extrapolated position of a charged track was not treated as an independent track.

Selection of multihadron final states from e^+e^- annihilation was based on the charged-particle momenta measured in the CDC and on the neutral-particle energy measured in the SHC. Multihadron-event selection in AMY is described in detail in Ref. 24. The main selection criteria include the following.

(1) Five or more charged tracks with $|\cos\theta| \leq 0.85$ originating from points within $r = 5$ cm and $|z| = 15$ cm of the interaction point.

(2) Total visible energy (E_{vis}) more than half of the total c.m. energy.

(3) Momentum imbalance along the beam direction with a magnitude less than $0.4E_{vis}$.

(4) More than 3 (5) GeV deposited in the SHC at 52 (55–57) GeV.

According to Monte Carlo calculations, the fraction of background from $e^+e^- \rightarrow \tau^+\tau^-$ and two-photon hadron events are 0.6–0.9% and 0.6–0.7% (Ref. 25) depending on the beam energy, respectively. The fraction of background contamination from beam-gas collisions is 0.3% (Ref. 24). To ensure a large acceptance for particles in the jets, only events with $|\cos\theta_{thrust}| < 0.7$ were considered, where θ_{thrust} is the angle between the thrust axis of the event and the beam axis. A total of 1911 events

TABLE III. Parameters for the Webber model (BIGWIG 4.3).

	Default	Mark II
Λ_{LLA} (GeV)	0.2	0.2
Cascade virtuality cutoff Q_0 (GeV)	0.65	0.75
Cluster mass parameter m_c (GeV/c ²)	5.0	3.0

TABLE IV. The rapidity Y distribution for charged particles with respect to the thrust axis, $(1/N_{ev})(dn/dY)$. [$N_{ev}(n)$ is the number of events (charged particles).] These data are plotted in Fig. 1.

Rapidity	Data
0.00–0.50	6.08±0.13
0.50–1.00	6.22±0.22
1.00–1.50	6.15±0.10
1.50–2.00	5.44±0.15
2.00–2.50	4.40±0.11
2.50–3.00	3.27±0.07
3.00–3.50	1.80±0.05
3.50–4.00	0.686±0.032
4.00–4.50	0.185±0.016
4.50–5.00	0.052±0.008

from an integrated luminosity of 18.63 pb^{-1} passed the selection criteria at c.m. energies from 52 to 57 GeV.

VI. DATA CORRECTION

To correct the observed distributions for detector acceptance, initial-state radiation effects, and the multihadron-event selection cuts, QCD Monte Carlo programs including fragmentation models are used to simulate multihadron events. In the first step, N_{gen} Monte Carlo events are generated without initial-state radiation. These events yield the distributions $n_{gen}(x)$, where x represents the variable of interest, of all long-lived particles produced either at primary vertices or from the decays of all short-lived states such as K_S^0 , strange baryons, resonances, and particles containing charm and bottom quarks. For the distributions of quantities that depend on particle masses, the known masses of the particles are used.

For the second step, events are generated including initial-state radiation²⁶ and traced through the AMY detector. Energy loss, multiple scattering, photon conversion, and nuclear interactions in the material of the detector, as well as decays, are taken into account. This information is then converted into the quantities measured by the detector (e.g., drift times and pulse heights).

TABLE V. The charged-particle X distribution, $(1/N_{ev})(dn/dX)$. These data are plotted in Fig. 2.

X	Data
0.00–0.10	134.34±0.98
0.10–0.20	23.51±0.39
0.20–0.30	7.79±0.22
0.30–0.40	3.17±0.15
0.40–0.50	1.23±0.09
0.50–0.60	0.532±0.050
0.60–0.70	0.310±0.038
0.70–0.80	0.124±0.022
0.80–0.90	0.021±0.006
0.90–1.00	0.0038±0.0018
Average	0.0747±0.0007

TABLE VI. The charged-particle P_L (GeV/c) distribution, $(1/N_{ev})(dn/dP_L)$ [(GeV/c)⁻¹]. These data are plotted in Fig. 3.

P_L	Data
0.00–1.60	7.14±0.07
1.60–3.20	1.74±0.03
3.20–4.80	0.770±0.020
4.80–6.40	0.408±0.014
6.40–8.00	0.251±0.011
8.00–9.60	0.123±0.007
9.60–11.20	0.0833±0.0059
11.20–12.80	0.0502±0.0045
12.80–14.40	0.0307±0.0035
14.40–16.00	0.0228±0.0030
Average	1.99±0.02

The events are then passed through the same reconstruction algorithms and analysis programs used for our experimental data. From the N_{det} accepted events are obtained the detected particle distributions $n_{det}(x)$.

The corrected distributions $dn_{cor}(x)$ as a function of a variable x are then obtained from the measured distributions $dn_{meas}(x)$ by using a bin-by-bin correction function $C(x)$:

$$dn_{cor}(x) = C(x)dn_{meas}(x),$$

where $C(x)$ is calculated by

$$C(x) = \frac{n_{gen}(x)/N_{gen}}{n_{det}(x)/N_{det}}.$$

This method was used to compute correction functions using different models and then the results were averaged. We chose to use the Lund parton-shower (PS) model and the Lund matrix-element (ME) model. The difference between the correction functions computed from average values and from the two models individually was taken as an estimate of the systematic uncertainty in the corrections. These uncertainties were typically on the order of, or smaller than, the statistical uncertainties, except for the tails of a few distributions, and were combined in

TABLE VII. The charged-particle P_T (GeV/c) distribution, $(1/N_{ev})(dn/dP_T)$ [(GeV/c)⁻¹]. These data are plotted in Fig. 4.

P_T	Data
0.00–0.50	22.78±0.19
0.50–1.00	7.84±0.10
1.00–1.50	2.014±0.048
1.50–2.00	0.757±0.028
2.00–2.50	0.307±0.017
2.50–3.00	0.151±0.012
3.00–3.50	0.0752±0.0082
3.50–4.00	0.0351±0.0056
4.00–4.50	0.0222±0.0044
4.50–5.00	0.0166±0.0037
Average	0.491±0.005

TABLE VIII. The charged-particle P_T^2 [(GeV/c)²] distribution, $(1/N_{ev})(dn/dP_T^2)$ [(GeV/c)⁻²]. These data are plotted in Fig. 5.

P_T^2	Data
0.00–1.00	15.31±0.10
1.00–2.00	0.898±0.025
2.00–3.00	0.333±0.013
3.00–4.00	0.147±0.009
4.00–5.00	0.0853±0.0064
5.00–6.00	0.0606±0.0054
6.00–7.00	0.0389±0.0043
7.00–8.00	0.0283±0.0036
Average	0.49±0.02

TABLE IX. The charged-particle P_T^{in} (GeV/c) distribution, $(1/N_{ev})(dn/dP_T^{in})$ [(GeV/c)⁻¹]. These data are plotted in Fig. 6.

P_T^{in}	Data
0.00–0.50	25.95±0.19
0.50–1.00	5.35±0.08
1.00–1.50	1.56±0.04
1.50–2.00	0.624±0.025
2.00–2.50	0.276±0.016
2.50–3.00	0.142±0.011
3.00–3.50	0.0705±0.0080
3.50–4.00	0.0319±0.0053
4.00–4.50	0.0234±0.0045
4.50–5.00	0.0161±0.0037
Average	0.390±0.005

TABLE X. The charged-particle P_T^{out} (GeV/c) distribution $(1/N_{ev})(dn/dP_T^{out})$ [(GeV/c)⁻¹]. These data are plotted in Fig. 7.

P_T^{out}	Data
0.00–0.50	31.07±0.21
0.50–1.00	2.62±0.07
1.00–1.50	0.197±0.027
1.50–2.00	0.025±0.006
2.00–2.50	0.0049±0.0019
2.50–3.00	0.0010±0.0007
Average	0.215±0.003

TABLE XI. The charged-particle $\langle P_T^{in} \rangle$ [(GeV/c)²] distribution, $(1/N_{ev})(dN/d\langle P_T^{in} \rangle)$ [(GeV/c)⁻²]. These data are plotted in Fig. 8.

$\langle P_T^{in} \rangle$	Data
0.00–0.50	1.59±0.04
0.50–1.00	0.267±0.015
1.00–1.50	0.069±0.007
1.50–2.00	0.032±0.005
2.00–2.50	0.018±0.003
2.50–3.00	0.005±0.002
3.00–3.50	0.002±0.001
3.50–4.00	0.0019±0.0009
4.00–4.50	0.0014±0.0008
4.50–5.00	0.0004±0.0004
Average	0.40±0.02

TABLE XII. The charged-particle $\langle P_T^{out} \rangle$ [(GeV/c)²] distribution, $(1/N_{ev})(dN/d\langle P_T^{out} \rangle)$ [(GeV/c)⁻²]. These data are plotted in Fig. 9.

$\langle P_T^{out} \rangle$	Data
0.00–0.10	7.31±0.21
0.10–0.20	1.92±0.15
0.20–0.30	0.32±0.06
0.30–0.40	0.062±0.016
0.40–0.50	0.0216±0.0070
0.50–0.60	0.0125±0.0048
0.60–0.70	0.0055±0.0032
0.70–0.80	0.0036±0.0026
Average	0.087±0.003

TABLE XIII. The charged-particle flow with respect to the sphericity axis, $(1/N_{ev})(dn/d\theta)$. These data are plotted in Fig. 10.

θ (deg)	Data
0.00–6.00	0.410±0.007
6.00–12.0	0.446±0.011
12.0–18.0	0.336±0.009
18.0–24.0	0.267±0.006
24.0–30.0	0.209±0.005
30.0–36.0	0.180±0.005
36.0–42.0	0.151±0.004
42.0–48.0	0.138±0.005
48.0–54.0	0.124±0.005
54.0–60.0	0.110±0.004
60.0–66.0	0.110±0.004
66.0–72.0	0.098±0.004
72.0–78.0	0.095±0.004
78.0–84.0	0.091±0.004
84.0–90.0	0.092±0.004
Average	29.8±0.6

TABLE XIV. The energy flow with respect to the sphericity axis, $(1/N_{ev})(dE/d\theta)$ (GeV/deg). These data are plotted in Fig. 11.

θ (deg)	Data
0.00–6.00	3.505±0.021
6.00–12.0	2.079±0.054
12.0–18.0	1.087±0.036
18.0–24.0	0.623±0.018
24.0–30.0	0.417±0.007
30.0–36.0	0.288±0.006
36.0–42.0	0.224±0.004
42.0–48.0	0.185±0.005
48.0–54.0	0.160±0.005
54.0–60.0	0.134±0.004
60.0–66.0	0.124±0.004
66.0–72.0	0.109±0.004
72.0–78.0	0.106±0.006
78.0–84.0	0.109±0.006
84.0–90.0	0.102±0.005
Average	16.4±0.2

TABLE XV. The thrust distribution, $(1/N_{ev})(dN/dT)$. These data are plotted in Fig. 12.

Thrust	Data
0.60–0.65	0.013±0.013
0.65–0.70	0.150±0.048
0.70–0.75	0.500±0.090
0.75–0.80	0.773±0.098
0.80–0.85	1.37±0.11
0.85–0.90	2.52±0.15
0.90–0.95	7.00±0.31
0.95–1.00	7.41±0.52
Average	0.917±0.002

TABLE XVI. The major-value distribution, $(1/N_{ev})(dN/dM_2)$. These data are plotted in Fig. 13.

Major value	Data
0.00–0.05	0.067±0.030
0.05–0.10	2.18±0.30
0.10–0.15	5.17±0.52
0.15–0.20	4.14±0.23
0.20–0.25	2.45±0.14
0.25–0.30	2.04±0.13
0.30–0.35	1.23±0.10
0.35–0.40	0.766±0.090

TABLE XVII. The minor-value distribution, $(1/N_{ev})(dN/dM_3)$. These data are plotted in Fig. 14.

Minor value	Data
0.00–0.05	0.523±0.076
0.05–0.10	7.68±0.33
0.10–0.15	7.24±0.45
0.15–0.20	2.34±0.40
0.20–0.25	0.65±0.15
0.25–0.30	0.300±0.059
0.30–0.35	0.075±0.020
0.35–0.40	0.017±0.010
Average	0.116±0.002

TABLE XVIII. The oblateness distribution, $(1/N_{ev})(dN/dO)$. These data are plotted in Fig. 15.

Oblateness	Data
0.00–0.05	8.73±0.42
0.05–0.10	5.31±0.22
0.10–0.15	2.59±0.15
0.15–0.20	1.44±0.12
0.20–0.25	0.821±0.089
0.25–0.30	0.435±0.066
0.30–0.35	0.271±0.054
0.35–0.40	0.201±0.050
Average	0.085±0.002

TABLE XIX. The sphericity distribution, $(1/N_{ev})(dN/dS)$. These data are plotted in Fig. 16.

Sphericity	Data
0.00–0.10	7.17±0.21
0.10–0.20	1.44±0.08
0.20–0.30	0.603±0.052
0.30–0.40	0.357±0.044
0.40–0.50	0.197±0.035
0.50–0.60	0.109±0.026
0.60–0.70	0.053±0.018
0.70–0.80	0.031±0.013
Average	0.095±0.003

TABLE XX. The aplanarity distribution, $(1/N_{ev})(dN/dA)$. These data are plotted in Fig. 17.

Aplanarity	Data
0.00–0.04	22.50±0.56
0.04–0.08	1.47±0.29
0.08–0.12	0.328±0.058
0.12–0.16	0.131±0.033
0.16–0.20	0.044±0.019
0.20–0.24	0.009±0.011
Average	0.0172±0.0008

TABLE XXI. The Q_x distribution, $(1/N_{ev})(dN/dQ_x)$. These data are plotted in Fig. 18.

Q_x	Data
0.00–0.10	0.058±0.021
0.10–0.20	0.101±0.025
0.20–0.30	0.249±0.037
0.30–0.40	0.581±0.053
0.40–0.50	1.54±0.08
0.50–0.60	7.51±0.21
Average	0.510±0.002

TABLE XXII. The Q_2-Q_1 distribution, $(1/N_{ev})[dN/d(Q_1-Q_2)]$. These data are plotted in Fig. 19.

Q_2-Q_1	Data
0.00–0.06	13.55±0.37
0.06–0.12	1.68±0.13
0.12–0.18	0.663±0.074
0.18–0.24	0.335±0.055
0.24–0.30	0.234±0.048
0.30–0.36	0.132±0.038
0.36–0.42	0.050±0.024
0.42–0.48	0.020±0.015
Average	0.040±0.002

quadrature with the statistical errors. The correction factors themselves were generally close to unity, lying mainly between 0.7 and 1.4.

Because of the limited number of events available at any single energy value, the data collected from the 52–57-GeV energy region were averaged to produce the distributions. The contribution of this combining procedure to the systematic error was neglected, as investigation by additional Monte Carlo analysis found it to be small, typically on the order of $\frac{1}{10}$ of the combined systematic and statistical errors. The combined data were assumed to correspond to data taken at an average center-of-mass energy of 55.2 GeV.

VII. COMPARISON WITH MODELS

The data distributions are shown and compared with the predictions of the Lund ME, Lund PS, and Webber models in Figs. 1–22. In Figs. 2 and 4, we also compare AMY data for X and P_T distributions with the Chou-Yang parametrization.²⁷ The default values of the relevant parameters as suggested by the authors of the programs are presented in Tables I–III along with the values optimized for Mark II data. The Mark II values were used in generating the distributions for the Lund ME and Webber models. In the case of the Lund PS, where there was little difference between the Mark II tuned and default values, the default values were retained. The default values of the models' secondary parameters were not altered or tuned. Values for AMY data points for nonzero bins are presented for all distributions in Tables IV–XXV. Also presented in these tables are the average values of selected observables as calculated from the data. Table XXVI gives a summary of the χ^2 values obtained by the comparison of each distribution to each of the three models.

The Lund ME model shows significant disagreement with AMY data when the Mark II parameters in Table I are used. The model has a deeper dip in rapidity (Fig. 1) at low Y and gives too many particles of high rapidity. Too many hard hadrons are predicted in the plots of X (Fig. 2) and P_L (Fig. 3), yet $Q_2 - Q_1$ (Fig. 19), related to the handling of hard-gluon radiation, is reproduced quite accurately. The model underestimates the regions of high P_T^{out} (Fig. 7), $\langle P_T^{\text{out}} \rangle$ (Fig. 9), minor value (Fig. 14), and aplanarity (Fig. 17). The thrust distribution (Fig. 12) is shifted slightly to higher values. It is possible to tune the parameters to obtain much better agreement for most of the distributions, but this requires driving some of

TABLE XXIII. The slim-jet scaled mass M_{sl}^2/s distribution, $(1/N_{\text{ev}})[dN/d(M_{\text{sl}}^2/s)]$. These data are plotted in Fig. 20.

M_{sl}^2/s	Data
0.00–0.04	20.62±0.52
0.04–0.08	3.80±0.25
0.08–0.12	0.80±0.15
0.12–0.16	0.056±0.042
Average	0.028±0.001

TABLE XXIV. The broad-jet scaled mass M_{br}^2/s distribution, $(1/N_{\text{ev}})[dN/d(M_{\text{br}}^2/s)]$. These data are plotted in Fig. 21.

M_{br}^2/s	Data
0.00–0.04	9.71±0.50
0.04–0.08	9.14±0.46
0.08–0.12	3.43±0.24
0.12–0.16	1.54±0.15
0.16–0.20	0.67±0.11
0.20–0.24	0.467±0.094
0.24–0.28	0.077±0.038
0.32–0.36	0.011±0.011
0.36–0.40	0.0033±0.0046
Average	0.063±0.002

them to extreme values. Even so, the model seriously underestimates the high P_T^{out} -related quantities. As has been pointed out,⁶ this deficiency is related to insufficient simulation of multigluon emission in the matrix-element approach. Summing over all the plots, the total χ^2 is 2783 for 196 data points using the Mark II parameter values, 1936 using TASSO's values,⁶ while 3343 is obtained by assuming the default parameter values. With the parameters tuned to AMY data, a χ^2 of 427 is obtained, but with an unrealistic value for $\Lambda_{\overline{\text{MS}}}$, listed in Table I (Ref. 28).

The Webber model as incorporated in BIGWIG 4.3 yields better agreement with AMY data when the Mark II parameters are used. These give a much better description than using the default BIGWIG parameters. The agreement was also better than that obtained from the more recent Marchesini-Webber program HERWIG 3.2, which, in addition, is able to describe events with a hadronic origin. (See Ref. 29 for a more detailed discussion of our comparison with HERWIG 3.2.) Specifically, the BIGWIG program gives the best reproduction of the rapidity distribution (Fig. 1) among the models examined. $Q_2 - Q_1$ (Fig. 19) is also well described, as are P_T (Fig. 4), P_T^{out} (Fig. 5), and P_T^{in} (Fig. 6). Nevertheless, the model still demands a surplus of spherical events, which appear as an excess of low thrust (Fig. 12) and high sphericity (Fig. 16) events. In addition, the $\langle P_T^{\text{in}} \rangle$ (Fig. 8) distribution is

TABLE XXV. The jet scaled mass difference $(M_{\text{br}}^2 - M_{\text{sl}}^2)/s$ distribution, $(1/N_{\text{ev}})[dN/d[(M_{\text{br}}^2 - M_{\text{sl}}^2)/s]]$. These data are plotted in Fig. 22.

$(M_{\text{br}}^2 - M_{\text{sl}}^2)/s$	Data
0.00–0.04	17.67±0.57
0.04–0.08	4.41±0.30
0.08–0.12	1.59±0.15
0.12–0.16	0.80±0.11
0.16–0.20	0.272±0.067
0.20–0.24	0.182±0.056
0.24–0.28	0.016±0.016
0.28–0.32	0.013±0.013
0.32–0.36	0.0074±0.0074
Average	0.035±0.001

TABLE XXVI. Summary of χ^2 for each model comparison to each distribution as shown in the figures: (a) Lund parton shower with default parameters, (b) Lund matrix element with Mark II parameters, (c) Webber model (BIGWIG 4.3) with Mark II parameters.

Figure number	Distribution	(a) χ^2 for Lund PS	(b) χ^2 for Lund MA	(c) χ^2 for Webber	Number of data points
1	Rapidity	52.3	309.2	25.6	10
2	X	13.7	197.1	18.2	10
3	P_L	18.4	135.5	17.0	10
4	P_T	30.3	175.1	29.5	10
5	P_T^2	19.5	112.5	19.3	8
6	P_T^{in}	26.5	97.0	23.4	10
7	P_T^{out}	5.6	239.9	33.3	6
8	$\langle P_T^{\text{in}2} \rangle$	12.4	20.1	28.6	10
9	$\langle P_T^{\text{out}2} \rangle$	6.8	115.4	53.3	8
10	Charged particle flow	63.5	324.7	21.5	15
11	Energy flow	45.0	575.1	131.4	15
12	Thrust	11.3	37.6	22.6	8
13	Major value	12.7	45.6	15.9	8
14	Minor value	8.4	187.4	43.8	8
15	Oblateness	3.7	14.4	7.2	8
16	Sphericity	3.4	29.4	12.1	8
17	Aplanarity	2.8	48.4	25.5	6
18	Q_x	2.6	20.5	12.0	6
19	$Q_2 - Q_1$	1.7	1.5	5.6	8
20	M_{sl}^2/s	2.9	50.3	12.1	4
21	M_{br}^2/s	13.4	26.6	15.5	9
22	$(M_{\text{br}}^2 - M_{\text{sl}}^2)/s$	14.8	19.8	27.1	9
	Total	371	2783	601	194

slightly overestimated in the high-momentum region. The model also overestimates the high-valued regions for P_T^{out} (Fig. 7), $\langle P_T^{\text{out}2} \rangle$ (Fig. 9), the minor value (Fig. 14), and aplanarity (Fig. 17), distributions which are sensitive to soft-gluon emission. Furthermore, the energy flow (Fig. 11) is underestimated in the region close to the jet axis and overestimated in the region 15° to 40° from the jet axis. With the Mark II and TASSO values, the total χ^2 are 601 and 1339, respectively, while BIGWIG 4.3 default values yield 5461.

The Lund parton-shower model gives in general a good description of AMY data, and, of the three models considered, yields the most satisfactory agreement, though with certain discrepancies. As it did at PEP and PETRA energies, Lund PS reproduces well the aplanarity, minor value, P_T^{out} and most of the other distributions. The rapidity distribution is predicted to have a slightly lower dip in the $Y \approx 0$ region and an excess of events with $Y > 2.0$. For $\theta > 30^\circ$, the charged-particle flow (Fig. 10) is underestimated while for $\theta > 60^\circ$, the particles are given insufficient energy (Fig. 11). This is consistent with the model's prediction of too many events with high thrust (Fig. 12). The model underestimates to some extent the high- P_T region of the P_T , P_T^{in} , and P_T^2 distributions. The overall χ^2 values are 372, 400, and 559 for the program's default parameters, Mark II-tuned parameters, and the TASSO-tuned parameters, respectively.

VIII. SUMMARY

We have studied multihadron events from e^+e^- annihilation at $\sqrt{s} = 52\text{--}57$ GeV with the AMY detector at TRISTAN. Event-shape, particle-flow, and inclusive particle distributions have been measured.

The data have been corrected for the effects of detector acceptance and initial-state radiation and compared with the Lund parton-shower, Lund matrix-element, and Webber (BIGWIG 4.3) QCD+fragmentation models. At TRISTAN energies, with the parameter values tuned for PEP and PETRA energies, Lund ME shows some large deviations and demonstrates significant difficulties in reproducing the experimental data for most of the event-shape distributions. On the other hand, both the Webber and the Lund PS models provide a good description of AMY data. In general, the Webber model gives a fairly good description of the P_T^{in} -related quantities, but reproduces less well the P_T^{out} -related distributions. The Lund PS, too, is in reasonable agreement with P_T^{in} distributions, yet also yields an accurate reproduction of P_T^{out} quantities. The total χ^2 of the fits following the Lund parton-shower approach is the lowest among the three models examined. From this point of view, the Lund parton-shower model passes a crucial test through its ability to describe data from different energy regions using a single set of parameters.

ACKNOWLEDGMENTS

We thank the TRISTAN staff for the excellent operation of the storage ring. In addition, we acknowledge the strong support and enthusiastic assistance provided by the staffs of our home institutions. This work has been

supported by the Japan Ministry of Education, Science and Culture (Monbusho), the Japan Society for the Promotion of Science, the U.S. Department of Energy and National Science Foundation, the Korea Science and Engineering Foundation and Ministry of Education, and the Academia Sinica of the People's Republic of China.

-
- ¹S. L. Glashow, Nucl. Phys. **22**, 579 (1961); S. Weinberg, *ibid.* **19**, 1264 (1967).
- ²D. Gross and F. Wilczek, Phys. Rev. Lett. **30**, 1343 (1973); H. D. Politzer, *ibid.* **30**, 1346 (1973); S. Weinberg, *ibid.* **31**, 494 (1973); H. Fritzsch, M. Gell-Mann, and H. Leutwyler, Phys. Lett. **47B**, 365 (1973).
- ³TASSO Collaboration, H. Althoff *et al.*, Z. Phys. C **22**, 307 (1984).
- ⁴HRS Collaboration, D. Bender *et al.*, Phys. Rev. D **31**, 1 (1985).
- ⁵Mark II Collaboration, A. Petersen *et al.*, Phys. Rev. D **37**, 1 (1988).
- ⁶TASSO Collaboration, W. Braunschweig *et al.*, Z. Phys. C **41**, 359 (1988).
- ⁷AMY Collaboration, H. Sagawa *et al.*, Phys. Rev. Lett. **60**, 93 (1988).
- ⁸AMY Collaboration, H. W. Zheng *et al.*, KEK Report No. 90-5 and University of Rochester Report No. UR-1155, 1990 (unpublished).
- ⁹JADE Collaboration, W. Bartel *et al.*, Phys. Lett. **101B**, 129 (1981); **134B**, 275 (1984); TPC Collaboration, H. Aihara *et al.*, Phys. Rev. Lett. **54**, 270 (1985).
- ¹⁰F. Gutbord, G. Kramer, and G. Schierholz, Z. Phys. C **21**, 235 (1984).
- ¹¹T. Sjöstrand and M. Bengtsson, Comput. Phys. Commun. **43**, 367 (1987).
- ¹²B. Andersson, G. Gustafsson, G. Ingelman, and T. Sjöstrand, Phys. Rep. **97**, 33 (1983).
- ¹³A general review of fragmentation models may be found in T. Sjöstrand, Int. J. Mod. Phys. A **3**, 751 (1988).
- ¹⁴T. Sjöstrand, Comput. Phys. Commun. **39**, 347 (1986).
- ¹⁵JADE Collaboration, W. Bartel *et al.*, Z. Phys. C **25**, 231 (1984); **33**, 23 (1986).
- ¹⁶S. Bethke, Heidelberg Habilitation Thesis, Report No. LBL 50-208, 1987; TASSO Collaboration, W. Braunschweig *et al.*, Phys. Lett. B **214**, 286 (1988).
- ¹⁷AMY Collaboration, I. H. Park *et al.*, Report No. KEK 88-45, 1988, (unpublished).
- ¹⁸M. Bengtsson and T. Sjöstrand, Phys. Lett. B **185**, 435 (1987).
- ¹⁹G. Fox and S. Wolfram, Phys. Rev. Lett. **41**, 1581 (1978); Nucl. Phys. **B149**, 413 (1979); Phys. Lett. **82B**, 134 (1979).
- ²⁰G. Altarelli and G. Parisi, Nucl. Phys. **B126**, 298 (1977).
- ²¹G. Marchesini and B. Webber, Nucl. Phys. **B238**, 1 (1984); B. Webber, *ibid.* **B238**, 492 (1984).
- ²²G. Marchesini and B. Webber, Nucl. Phys. **B310**, 461 (1988); B. Webber (private communication).
- ²³For the determination of these quantities in the analysis, we divide the mass squared by the visible energy squared E_{vis}^2 rather than by s , assuming a pion mass for all charged particles measured in the AMY detector.
- ²⁴AMY Collaboration, T. Mori *et al.*, Phys. Lett. B **218**, 499 (1989).
- ²⁵T. Mori, thesis, University of Rochester, Report No. UR-1104, 1988.
- ²⁶F. Berends, R. Kleiss, and S. Jadach, Z. Nucl. Phys. **202**, 63 (1982); Comput. Phys. Commun. **29**, 1985 (1983).
- ²⁷T. T. Chou and C. N. Yang, Phys. Lett. B **212**, 185 (1988); T. T. Chou (private communication).
- ²⁸Experiments have shown $\Lambda_{\overline{\text{MS}}}$ to be within the approximate range 100–400 MeV [T. Kamae, in *Proceedings of the 24th International Conference on High Energy Physics*, Munich, West Germany, 1988, edited by R. Kotthaus and J. H. Kühn (Springer, Berlin, 1988)].
- ²⁹AMY Collaboration, Y. K. Li *et al.*, in *Proceedings of the XIVth International Symposium on Lepton and Photon Interactions*, Stanford, California, 1989, edited by M. Riordan (World Scientific, Singapore, in press).